

# **Water Resources Research**

## **RESEARCH ARTICLE**

10.1002/2013WR014603

#### **Kev Points:**

- Subsurface preferential flow was noninvasively mapped by time-lapse
- Standardized radargram differences pinpointed preferential flow location
- Soil water monitoring confirmed the locations of lateral preferential flow

## **Supporting Information:**

- Readme
- Figure S1
- Figure S2
- Figure S3
- Figure S4
- Table S1

## **Correspondence to:**

H. Lin, henrylin@psu.edu

#### Citation:

Guo, L., J. Chen, and H. Lin (2014), Subsurface lateral preferential flow network revealed by time-lapse ground-penetrating radar in a hillslope, *Water Resour. Res.*, *50*, 9127–9147, doi:10.1002/ 2013WR014603.

Received 17 AUG 2013 Accepted 20 OCT 2014 Accepted article online 27 OCT 2014 Published online 1 DEC 2014

# Subsurface lateral preferential flow network revealed by time-lapse ground-penetrating radar in a hillslope

Li Guo<sup>1,2,3</sup>, Jin Chen<sup>1,2</sup>, and Henry Lin<sup>3</sup>

<sup>1</sup>State Key Laboratory of Earth Surface Processes and Resources Ecology, Beijing Normal University, Beijing, China, <sup>2</sup>College of Global Change and Earth System Science, Beijing Normal University, Beijing, China, <sup>3</sup>Department of Ecosystem Science and Management, Pennsylvania State University, University Park, Pennsylvania, USA

Abstract Subsurface lateral preferential flow (LPF) has been observed to contribute substantially to hillslope and catchment runoff. However, the complex nature of LPF and the lack of an appropriate investigation method have hindered direct LPF observation in the field. Thus, the initiation, persistence, and dynamics of LPF networks remain poorly understood. This study explored the application of time-lapse ground-penetrating radar (GPR) together with an artificial infiltration to shed light on the nature of LPF and its dynamics in a hillslope. Based on our enhanced field experimental setup and carefully refined GPR data postprocessing algorithms, we developed a new protocol to reconstruct LPF networks with centimeter resolution. This is the first time that a detailed LPF network and its dynamics have been revealed noninvasively along a hillslope. Real-time soil water monitoring and field soil investigation confirmed the locations of LPF mapped by time-lapse GPR surveys. Our results indicated the following: (1) Increased spatial variations of radar signals after infiltration suggested heterogeneous soil water changes within the studied soil, which reflected the generation and dynamics of LPF; (2) Two types of LPF networks were identified, the network at the location of soil permeability contrasts and that formed via a series of connected preferential flow paths; and (3) The formation and distribution of LPF networks were influenced by antecedent soil water condition. Overall, this study demonstrates clearly that carefully designed time-lapse GPR surveys with enhanced data postprocessing offer a practical and nondestructive way of mapping LPF networks in the field, thereby providing a potentially significant enhancement in our ability to study complex subsurface flow processes across the landscape.

## 1. Introduction

Subsurface lateral preferential flow (LPF) often occurs when percolating water in a soil profile encounters a hydrologically restrictive layer (such as an impeding soil layer or a soil profile with contrasting textures or a low-permeable bedrock) [Luxmoore, 1990; Newman et al., 1998; Weiler et al., 2006; Allaire et al., 2009; Zhu and Lin, 2009; Graham et al., 2010]. LPF can also occur via a series of connected macropores or pipes that can deliver substantial amount of water downslope [Sidle et al., 2001; Burke and Kasahara, 2011; Graham and Lin, 2012]. Knowledge of LPF, including its formation, duration, network, and controls, is crucial for understanding aquifer recharge, storm water management, contaminant transport, nutrient distribution, and other hydrological and biogeochemical processes [Uhlenbrook, 2006; Jones, 2010; Lin, 2010; Zhang et al., 2011; Nimmo, 2012; Graham and Lin, 2012].

However, because of its occurrence in the hidden subsurface and the complex and dynamic nature of the nonuniform flow, LPF and its network remain challenging to be directly monitored and quantified *in situ* [Allaire et al., 2009; Zhang et al., 2011; Graham and Lin, 2012]. Traditional methods of studying LPF are largely destructive and based on interpolation between point-based measurements, such as hillslope trenching, soil excavation, and tracer (or irrigation) experiment [e.g., Tsuboyama et al., 1994; Wilcox et al., 1997; Noguchi et al., 2001; Anderson et al., 2009; Graham et al., 2010]. Such interpretations from the invasive methods are likely to be affected by the characteristics of the method used and the study site representativeness [Tromp-van Meerveld et al., 2007; van Verseveld et al., 2009; Zhang et al., 2011].

Recently, the application of noninvasive geophysical techniques (e.g., ground-penetrating radar or GPR, electromagnetic induction or EMI, and electrical resistivity tomography or ERT) has provided new opportunities for *in situ* LPF mapping with high spatial and temporal resolutions [e.g., *Yoder et al.*, 2001; *Holden*, 2004;

Zhu et al., 2010a, 2010b; Doolittle et al., 2012]. Among the different techniques, GPR offers the best possible spatial resolution.

Ground-penetrating radar transmits electromagnetic (EM) waves to detect changes in physical properties (especially the dielectric constant,  $\varepsilon$ ) within the shallow subsurface [Daniels, 1996]. GPR can be applied either directly or indirectly to map LPF in situ. For indirect LPF mapping, GPR is first used to identify subsurface cavities (such as soil pipes and macropores), and LPF pathways are then inferred from the hydrological connectivity of lateral subsurface pipes or macropores [e.g., Holden and Burt, 2002; Gormally et al., 2011]. Direct GPR-based LPF detection utilizes the sensitivity of EM energy (both wave velocity and reflection strength) to subsurface water variation. For low conductive, nonmagnetic, and nonsaline soils, as is the case in this study, the propagation velocity of EM wave can be approximated by the following equation:

$$V \approx \frac{c}{\sqrt{\varepsilon'}},$$
 (1)

where V is the propagation velocity of EM wave,  $\varepsilon'$  is the dielectric constant of the soil, and c is the speed of light in vacuum [Conyers and Goodman, 1997]. The soil water content is the dominant control of soil dielectric constant [Topp et al., 1980], which, in turn, determines the velocity and reflectivity of the EM wave transmitted by GPR [Huisman et al., 2003]. In practice, soil dielectric constant values (derived from the measured wave velocities by equation (1) can be quantitatively converted to soil water contents by empirical models, such as the Topp's equation [Topp et al., 1980] and Roth's equation [Roth et al., 1992]. Previous studies have validated GPR as an effective method to map near-surface soil water distribution [Huisman et al., 2003; Annan, 2005; Zhang et al., 2014].

An advance in mapping soil water distribution using GPR involves capturing subsurface water dynamics by repeated surveys. Because the internal architecture of the soil remains fairly unchanged throughout individual precipitation (or artificial infiltration) events or even seasonally, different wave velocities and reflectivities between repeated GPR surveys can be attributed to changes in soil water. Therefore, such radar signal differences can be used to study subsurface hydrological dynamics. For example, based on the GPR velocity differences (measured by picking corresponding reflections from repeated GPR surveys), *Truss et al.* [2007] and *Harrder et al.* [2011] mapped the subsurface wetting zones. By comparing radargrams before and after infiltration, *Trinks et al.* [2001] detected the vertical water migration from the increase in reflection strength below an infiltration intake area. During an extended infiltration experiment, *Grote et al.* [2005] combined the information on travel time and reflection of radar waves to monitor the variations in soil water and locate the subsurface areas with high water contents.

However, direct GPR-based LPF mapping has been restrained. Only *Holden* [2004] successfully detected LPF passing through soil pipes using repeated GPR surveys together with tracer injection. Furthermore, *Doolittle et al.* [2012] directly captured LPF pathways in soils and fractured shales by comparing radar scans before and after introducing water using a line source of infiltration.

Ideally, the radar signal differences between repeated radargrams can pinpoint positions where soil water has changed. However, due to the ground roughness and slope, repeating GPR surveys with identical geometry under *in situ* conditions is fairly challenging [*Truss et al.*, 2007]. The geometric mismatch between repeated radargrams can also lead to reflection differences, which are difficult to separate from those caused by soil water changes. Even using the most advanced repeated GPR survey strategy coupled with a precise positioning system, *Truss et al.* [2007] could only guarantee the repeatability of 2-D radargrams on the horizontal axis (i.e., the surface location direction), but failed to ensure the repeatability on the vertical axis (i.e., the travel time or wave propagating depth direction). Thus, information on the reflection differences between repeated radargrams was not fully utilized in that study. Moreover, even under laboratory conditions, subtracting an initial (preinfiltration) survey from the postinfiltration surveys collected with perfect repeatability would still produce strong reflection differences in zones unaffected by fluid infiltration, because the travel time shifts cumulate after a GPR wave passes a wetting zone [*Trinks et al.*, 2001; *Versteeg*, 2002; *Truss et al.*, 2007]. Therefore, improving the coherence between repeated radargrams (on both the vertical and horizontal directions) is urgently needed for reliable LPF detection using time-lapse GPR.

The purpose of this study was to develop a new protocol for detecting LPF paths in the field using timelapse GPR with refined resolution and accuracy, thus providing a means of reconstructing the LPF network and capturing its dynamics. First, we established a field experimental setup that combined an artificial infiltration and densely spaced GPR transects in a hillslope. Then, we developed an enhanced GPR data post-processing algorithm to normalize the repeated radargrams into the same geometry, hence ensuring the feasibility of reflection difference comparison between time-lapse surveys. Third, we established several criteria to define the extraction of macropore LPF signatures and the location of macropore LPF paths on the subtracted radargrams. Fourth, we developed a branch-node mapping algorithm to connect LPF detections on 2-D radargrams to a 3-D reconstruction of the LPF skeleton network. Interpretations from time-lapse GPR surveys were then compared with field soil investigations and real-time soil water content measurements for validation. The proposed noninvasive GPR-based LPF detection protocol can enhance the *in situ* study of the initiation, duration, network, and dynamics of LPF, thus providing a means of revealing subsurface flow processes in hillslopes.

## 2. Methodology

#### 2.1. Study Site

Field experiments were conducted in the Shale Hills Critical Zone Observatory, a small (7.9 ha) forested catchment located in central Pennsylvania, USA. The GPR survey grids were located in the middle of a concave hillslope (a swale, with a local slope of 14%), with the soil being the Rushtown series (*loamy-skeletal over fragmental, mixed, mesic Typic Dystrochrepts*) (Figure 1a). These are deep soils (> 2 m) with fractured shale bedrocks beneath, including the following horizons: Oe, 0–0.05 m; A, 0.05–0.12 m (silt loam); Bw, 0.12–0.45 m (silt loam); BC, 0.45–0.90 m (silty clay loam); C, 0.90–1.78 m (silty clay loam); and R, > 2 m (Figure 1b). Many root channels were distributed in the Oe to Bw horizons, and a dense layer was observed in the BC horizon (Figure 1b). More details about the study site and the soil series studied can be found in *Lin* [2006] and *Zhang et al.* [2014]. According to our previous electromagnetic induction (EMI) surveys in the Shale Hills, apparent electrical conductivity (EC<sub>a</sub>) of the Rushtown soil varied from  $\sim$ 6 mS/m in the wet season (spring) to  $\sim$ 2 mS/m in the dry season (autumn) [*Doolittle et al.*, 2012]. We have conducted numerous GPR investigations in this catchment [e.g., *Doolittle et al.*, 2012; *Zhang et al.*, 2014] and the previous results helped inform the design and interpretation in this study.

Field experiments were conducted on 21 July 2012, after a series of prior GPR tests and investigations in the catchment. No precipitation was recorded in one week before and during the experimental period. After the leaf litter layer (Oe) was cleared, a 2.5 m  $\times$  0.8 m survey grid consisting of 9 parallel survey lines with 0.1 m intervals was established perpendicular to the downslope direction (Figure 1c). Both ends of these survey lines were anchored tightly into ground by plastic stakes. An infiltration trench (1.0 m long  $\times$  0.2 m deep  $\times$  0.2 m wide; Figure 1c, middle left) and a soil pit (1.0 m long  $\times$  0.6 m deep  $\times$  0.2 m wide; Figure 1c, bottom left) were excavated 0.5 m upslope and 0.5 m downslope from the survey grid, respectively. A total of 15 ECH2O-5TE soil moisture and temperature probes (5 cm long  $\times$  3.8 cm wide  $\times$  0.7 cm thick; Decagon Devices, Inc., Pullman, WA) were installed on the upslope section of the soil pit at three depths corresponding to the A, Bw, and BC horizons (Figure 1c). Five replicated probes at each of the three depths allowed an improved capture of flow variability, which aided the identification of preferential flow signatures. Another five probes were installed on the downslope section of the infiltration trench to record soil water variation near the infiltration source area (Figure 1c). All probes were connected to EM50 dataloggers (Decagon Devices, Inc., Pullman, WA) to monitor real-time soil water dynamics at 1 min intervals.

# 2.2. Infiltration and Time-Lapse GPR Surveys

A 0.9 m long PVC pipe (0.1 m in diameter, with a longitudinal 0.9 m long  $\times$  0.03 m wide incision) was settled in the infiltration trench. Both ends of the PVC pipe were sealed with plastic caps. Before infiltration, two time-lapse GPR surveys were conducted to obtain the initial soil condition and to test the coherence of radargrams after data postprocessing (Table 1). The soil moisture probes showed that at the start of the experiment, the average soil water content of the study site was 0.225 m<sup>3</sup>/m<sup>3</sup>, with limited variation at different depths (Figure 2).

During infiltration, regular tap water was first pumped into the PVC pipe. After filling the pipe, water flowed out from the incision into the trench evenly and infiltrated into the subsurface. A constant water head (10 cm) was maintained by controlling the flow velocity with a pump during the infiltration. No overland flow was observed for the whole experimental duration. Five repeated GPR surveys were conducted at 5,

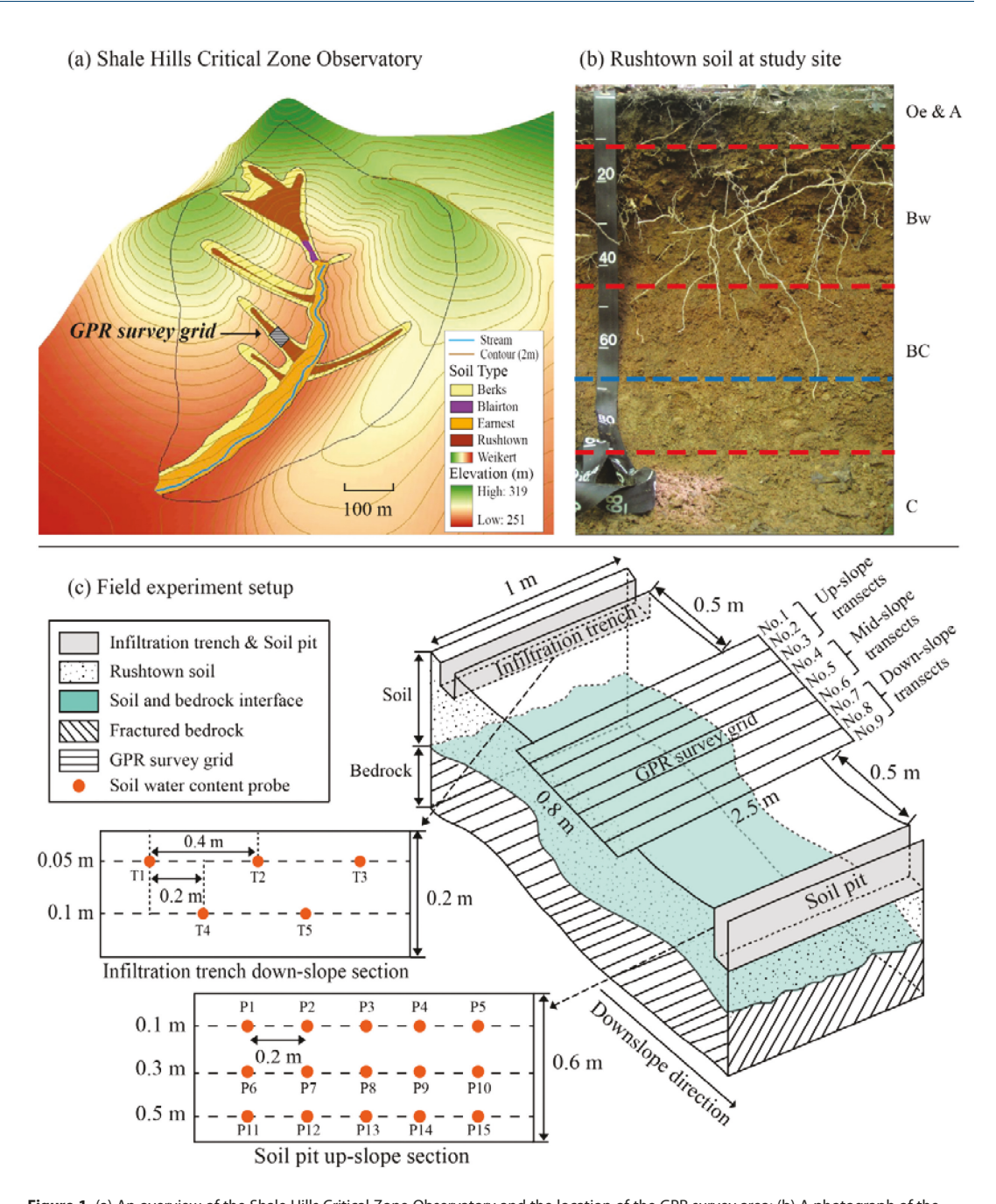


Figure 1. (a) An overview of the Shale Hills Critical Zone Observatory and the location of the GPR survey area; (b) A photograph of the Rushtown soil series at the study site, showing protruding lateral tree roots (especially in the Bw horizon), a dense layer of BC horizon (starting at the blue dashed line), and approximate interfaces between the different soil horizons (red dashed lines); and (c) The schematic of the infiltration experimental setup in this study.

15, 30, 45, and 60 min after the first 53 L of water drained completely from the infiltration trench (Table 1). Three more GPR surveys were conducted at 5, 15, and 30 min after the second 53 L of water was infiltrated (which was started 1 h and 28 min after the completion of the first infiltration; Table 1). In total, 90 radargrams (10 repeated surveys  $\times$  9 transects in each survey) were collected (see Table 1 for the detailed record of data collection). The soil water content and temperature near the infiltration trench are illustrated in Figure 2.

Radar data were collected using a Mala ProEx GPR system (Mala Geoscience, Mala, Sweden) equipped with shielded 800 MHz antennas (with the offset between transmitter and receiver fixed at 14 cm). The 800 MHz antennas, which provided the optimal trade-off between image resolution and detection depth for our

Table 1. Timing and Sequence of Events During the Field Experiment Conducted in this Study **GPR Survey Number** 13:10-13:22 First Prewetting background GPR survey 13:25-13:37 Second Repeat of prewetting GPR survey 13:38-13:50 Infiltration of 53 L water Third 13:51-13:57 GPR survey immediately after the first infiltration 14:06-14:13 Fourth GPR survey at 15 min after the first infiltration 14:21-14:28 Fifth GPR survey at 30 min after the first infiltration 14:36-14:42 Sixth GPR survey at 45 min after the first infiltration 14:51-14:59 Seventh GPR survey at 60 min after the first infiltration 15:18-15:51 Infiltration of another 53 L water 15:53-16:00 Eiahth GPR survey immediately after the second infiltration 16:08-16:13 GPR survey at 15 min after the second infiltration Ninth 16:23-16:28 Tenth GPR survey at 30 min after the second infiltration

study site, were chosen based on *in situ* testing of antennas with center frequencies ranging from 200 to 2300 MHz. The following parameters were fixed for radar data acquisition after preliminary tests: time window, 44 ns; stacking, 2; sampling interval, 0.0873 ns; and total samples per trace, 504. An odometer (with a diameter of 15 cm)

was used to trigger data collection at 1 cm intervals after *in situ* calibration. Due to the uneven topography in the hillslope, it is difficult to drag the antennas along each survey transect via the same distance. For each 2.5 m long survey transect,  $248 \sim 256$  traces were recorded.

A stainless steel plate (10 cm long  $\times$  10 cm wide  $\times$  0.5 cm thick) was inserted into a previously prepared soil pit at 0.5 m deep in the same Rushtown soil several meters away from the survey grid. In this way, the soil on top of the metal plate remained undisturbed. Radargrams were collected over the metal reflector. GPR wave velocity (9.12 cm/ns) was calculated as the ratio of metal plate depth (0.5 m) to the travel time interval from the ground surface to the soil-metal plate interface (5.48 ns; supporting information Appendix Figure 1). Given the limited water content variation at different soil depths, wave velocity was assumed to be constant across soil depths. Wave velocity was supported by the analysis of diffraction hyperbolae on radargrams (i.e., hyperbola fitting), which resulted in a very close velocity estimation, 9.20 cm/ns. Then, the vertical scale of radargram was converted from travel time to penetration depth based on the estimated wave velocity.

# 3. GPR Data Processing and Interpretation

Our GPR data processing and analysis procedures included five primary steps: (1) basic processing, (2) radargram standardization, (3) geometric match checking, (4) 3-D migration, and (5) lateral preferential flow detecting and mapping. The flowchart of our data processing and analysis procedures is illustrated in Figure 3, with each step detailed in the following subsections.

#### 3.1. Basic Processing

Several basic GPR data processing steps (including detrending, dewow, gain, frequency filtering, and background removal) were conducted to enhance the signal/noise ratio on the collected radargrams.

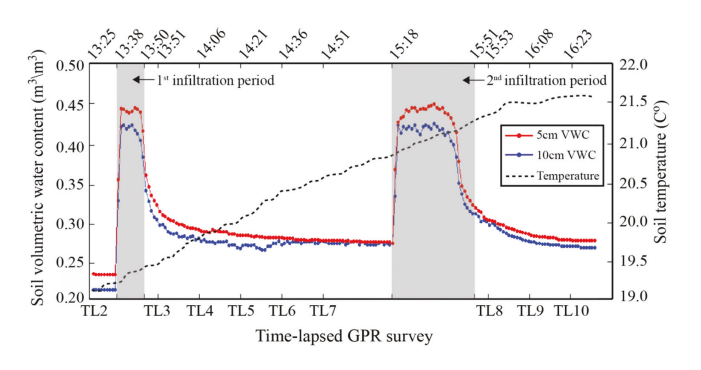


**Figure 2.** Time series of volumetric soil water content (WWC, average of each 5 and 10 cm depths, respectively) and soil temperature (average of all probes at the two depths) recorded in real-time at the upslope infiltration trench. TL stands for time-lapse GPR survey, followed by the number of survey sequence; TL3 to TL7 refers to 5, 15, 30, 45, and 60 min after the first infiltration; and TL8 to TL10 refers to 5, 15, and 30 min after the second infiltration.

1. Detrending was used to remove the radar data of the air layer and calibrate the effect of temperature drift by picking the first break on each trace [Truss et al., 2007]. One common method for automatic first break picking is the energy ratio method, which calculates the energy (i.e., the quadratic sum of amplitudes) in two successive equal length windows and locates the first break time when the energy ratio between the preceding and following windows reaches the minimum [Boschetti et al., 1996]. To avoid the random first break jitters calculated with a

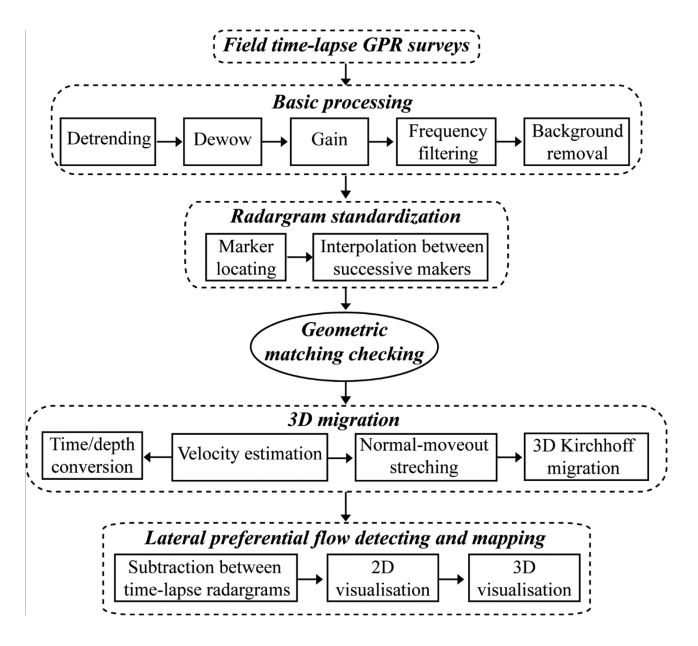


Figure 3. The flowchart of the GPR data processing steps developed in this study.

specific window length, we averaged the first break time obtained using 5 window sizes on each trace (i.e., 6, 8, 10, 12, and 14-sample wide, corresponding to 0.53, 0.70, 0.87, 1.05, and 1.22 ns wide, respectively). Given the surface topographic continuity among neighboring traces, the first breaks were then spatially smoothed to further eliminate the random first break jitters:

$$T_{j}' = \sum (0.25T_{j-2} + 0.5T_{j-1} + T_{j} + 0.5T_{j+1} + 0.25T_{j+2})/2.5,$$
(2)

where  $T_j$  is the smoothed first break time for the jth trace, and  $T_j$ is the first break time for the jth trace picked using the energy ratio method. Then, the smoothed first

break was aligned as the start of each trace throughout each radargram. Detrending suppressed the effects of uneven topography and bad coupling between the antenna and ground surface.

- 2. Dewow (or subtract mean), similar to DC-drift removal, was used to remove very low-frequency noise and correct the average amplitude of each trace approximating zero.
- 3. Radar reflection amplitude decays exponentially with propagation time [al Hagrey, 2007; Schmelzbach et al., 2012]. The measured amplitude, A(t), and the compensated amplitude without energy attenuation,  $A_0(t)$ , have the following relationship [Schmelzbach et al., 2012]:

$$A(t) = A_0(t) \left(\frac{1}{\sqrt{t}}\right) \exp\left(-\alpha^* t\right),\tag{3}$$

where t is the travel time of radar wave, and  $\alpha^*$  is an attenuation factor that determines the extent of radar energy attenuation. For a heterogeneous soil (such as the Rushtown soil in this study),  $\alpha^*$  changes with soil depth. Different from previous studies [e.g., Truss et al., 2007] that applied the same gain curve to all radargrams collected from different survey transects, we applied a specific gain curve to calibrate energy attenuation for repeated radargrams collected on each transect. Strictly speaking, even the gain curve for the same transect from different time-lapse surveys should be independent (because the infiltrated water changed the attenuation factor to different extents across all surveys). However, to avoid the noise signals caused by the application of different gain curves to the same transect, we used the gain curve obtained under the initial soil condition (i.e., before infiltration) to compensate for radar energy decay for each transect across all time-lapse surveys. First of all, the radar reflection amplitudes on each reference radargram (i.e., radargrams collected in the first survey) were converted to the corresponding envelopes by Hilbert transformation after Dewow. A mean decay curve was determined by summing all traces into one trace. Then, an exponential regression between the Hilbert-transformed amplitudes and travel times was established in successive regression windows. The fixed exponential parameter in the regression model was set as  $\alpha^*$  for the specific travel time corresponding to the middle sample of one regression window, resulting in a gain curve for each reference radargram. Finally, the compensated amplitude was recovered using equation (3) after Dewow. Other effective gain methods can also be adopted as alternatives to compensate the energy decay in GPR amplitudes.

- 4. Frequency filtering removed both high-frequency and low-frequency noise.
- 5. Background removal wiped off the horizontal banding signals (considered as background pulse or noises) that were never changed across each radargram.

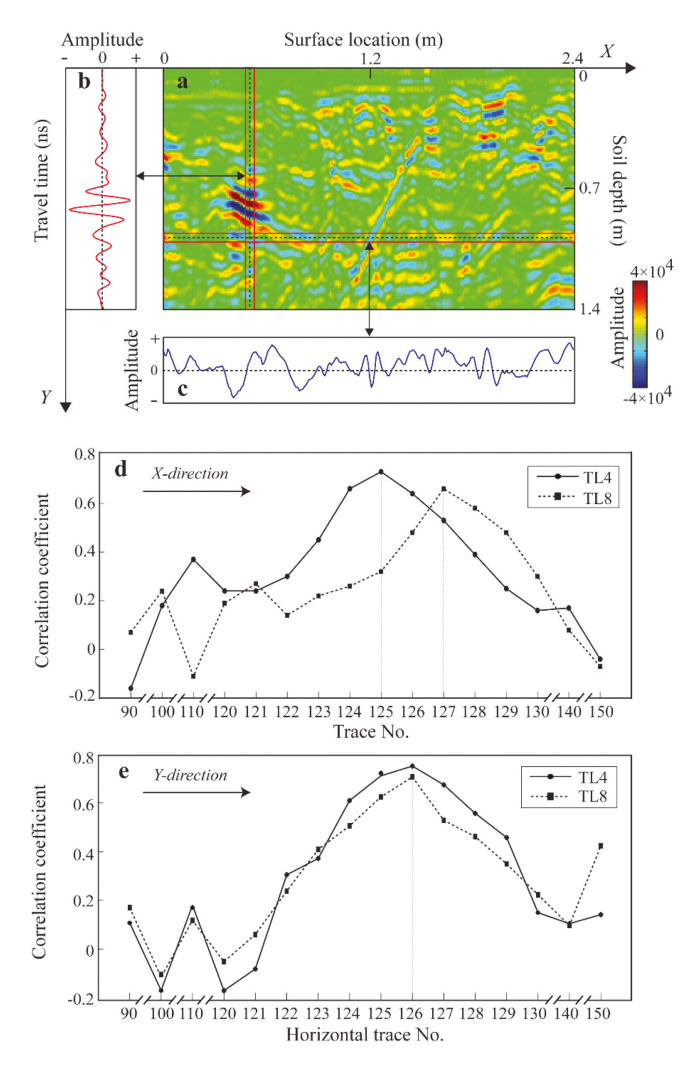


**Figure 4.** An example of radargram after the basic processing with travel time in the *Y* direction and surface location in (a) the *X* direction, (b) a vertical trace, and (c) a "horizontal trace". Also shown are correlation coefficients (d) between the repeated GPR surveys for the vertical marker trace (i.e., trace no. 125) and traces over the same transects but in subsequent GPR surveys (i.e., the fourth and eighth time-lapse surveys, TL4 and TL8) and (e) between the "horizontal marker trace" (i.e., "horizontal trace" no. 125) and "horizontal traces" over the same transects but in subsequent GPR surveys.

Dewow, frequency filtering, and background removal were performed with standard modules in Reflex-Win 6.1 GPR data processing software (Sandmeier Scientific Software, Karlsruhe, Germany). The improved algorithms of detrending and gain were coded using MATLAB (The MathWorks, Inc., Natick, MA, USA).

## 3.2. Radargram Standardization

Field-collected radargrams portray the nature of the investigated soil with travel time (or penetrating depth) in the Y direction and the surface location in the X direction (Figure 4a). The objective of radargram standardization is to normalize the repeated radargrams collected from the same survey transect into an identical geometric scale.

For X direction standardization, 25 spatially equidistant traces (trace no. 5, 15, 25 . . . 225, 235, and 245; with 10 cm intervals) were set as the marker traces on each reference radargram (i.e., radargrams collected in the first survey before infiltration). The next step was to locate the corresponding positions of markers on the repeated radargrams. Treating each radar trace as a time series of reflection amplitudes (Figure 4b), we calculated the correlation coefficients of the amplitudes between the marker trace on reference radargram and the traces on the repeated radargrams. The trace that achieved the maximum correlation coefficient with the marker trace was determined as the cor-

responding marker on each repeated radargram. For example, Figure 4d illustrates the correlation coefficients between trace no. 125 (the 13th marker on the reference radargram) collected from the first transect and the traces (from no. 90 to 150) on radargrams collected from the same transect but in the fourth and eighth surveys. In this case, trace no. 125 of the fourth survey and trace no. 127 of the eighth survey reached the strongest correlations with the marker trace, which were then determined accordingly as the 13<sup>th</sup> marker on the repeated radargrams collected in the fourth and eighth surveys, respectively (Figure 4d).

A 21-trace wide (i.e., 20 cm) search window was created on the repeated radargrams for the automatic location of marker position. Marker position (the surface location) on the reference radargram was set as the center of each search window. 20 cm was sufficiently wide to locate the corresponding marker position, as the marker trace was unlikely to deviate 10 cm away from its original position on the subsequent repeated radargrams. To improve the robustness of correlation comparison, the marker trace combined with the left and right traces were joined into one "long trace," and the correlation coefficients were calculated between the "long trace" and three successive traces within the search window. The middle trace of the three successive traces, where the highest correlation coefficient was obtained, was set as the corresponding marker

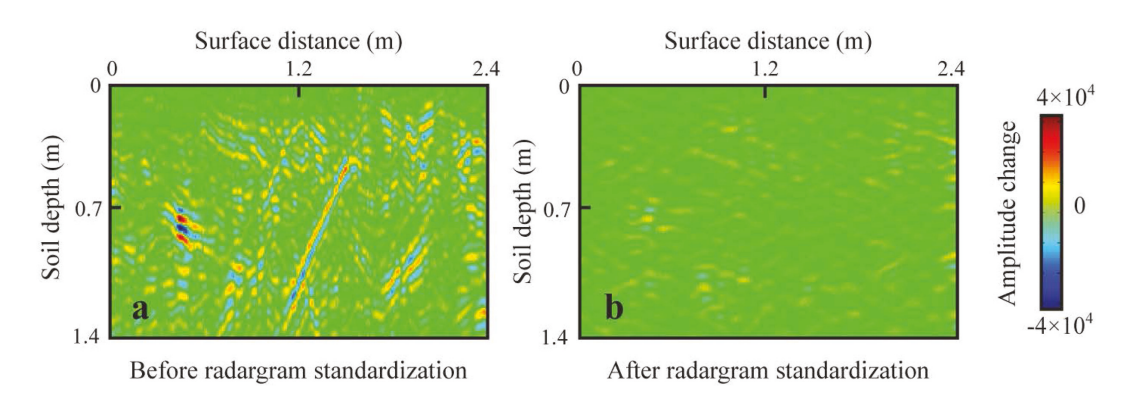


**Figure 5.** (a) Reflection difference between radargrams collected in two repeated GPR surveys before infiltration over the first survey transect, but without radargram standardization. (b) Reflection difference between the corresponding radargrams after standardization.

trace on the repeated radargrams. For our data, the horizontal shift of a maker trace could be as large as 5 cm.

After all 25 markers were located on each repeated radargram, we linearly interpolated the radar data in the *X* direction into the same spatial scale: 10 traces between successive markers and 1 cm intervals between neighboring traces. Before interpolation, the counts of traces between successive markers on the repeated radargrams ranged from 7 to 13 with a majority varying from 9 to 11. Thus, the interpolation of original traces did not significantly change the shape of the onsets. After trace interpolation and removing the traces outside the first and the last markers, each processed radargram (including the reference radargrams) contained 241 equidistant traces (i.e., 2.4 m in the *X* direction).

Before *Y* direction standardization, data collected later than 15.01 ns were removed from all radargrams because of the low signal/noise ratio in such deep soils. We defined the GPR data collected at same travel time across all traces on each radargram as a "horizontal trace" (i.e., a series of amplitudes changing with surface location; see an example in Figure 4c). Similar to the *X* direction standardization, correlation coefficients of amplitudes between the "horizontal trace" on reference radargrams and those on the repeated radargrams were calculated, and the marker position was then located on the corresponding subsequent radargrams. Figure 4e illustrates the correlation coefficients between "horizontal trace no. 125" on the reference radargram collected at 10.91 ns for the first transect and the "horizontal traces" (from no. 90 to 150) on repeated radargrams collected from 7.86 to 13.10 ns for the same transect but in the fourth and eighth surveys. For both the repeated surveys, "horizontal trace no. 126" collected at 11.00 ns displays the maximum correlation with the reference horizontal trace, implying a one-sample (i.e., 0.087 ns) delay on the repeated radargrams.

"Horizontal trace no. 40, 100, and 160" were set as the horizontal markers on the reference radargrams to represent the shallow, medium, and deep soil depths, respectively. The vertical position shifts of each marker on the subsequent repeated radargrams are listed in supporting information Appendix Table 1. 64% of the selected "horizontal markers" did not shift at all, 94% shifted within one sample, and no "horizontal marker" shifted more than two samples. Moreover, no accumulated vertical shift was observed for data collected at later travel times, indicating no significant travel time shift on the vertical axis (supporting information Appendix Table 1). Therefore, we stacked two successive samples on each trace using their mean value. In this manner, the mismatching in the Y direction was corrected. Ideally, horizontal traces are recommended to choose for the strong reflections from boundaries between soil layers. But if the stratigraphy is not horizontally distributed, which is the common case in a hillslope, it is difficult to select a horizontal trace exactly crossing a boundary between soil layers. Hence, like the setting of vertical maker traces, several spatially equidistant horizontal traces corresponding to different soil depths can be chosen as the horizontal trace markers.

After radargrams standardization, all radargrams were normalized in the same dimension: 241 equidistant traces with 1 cm intervals in the *X* direction and 15.01 ns (or 86 samples with an interval of 0.175 ns) per trace in the *Y* direction. Standardization was achieved using the code we developed in MATLAB.

## 3.3. Geometric Matching Check

The goal of the geometric matching check was to evaluate the geometric coherence among the normalized time-lapse radargrams. Direct subtraction between corresponding radargrams collected in the first two

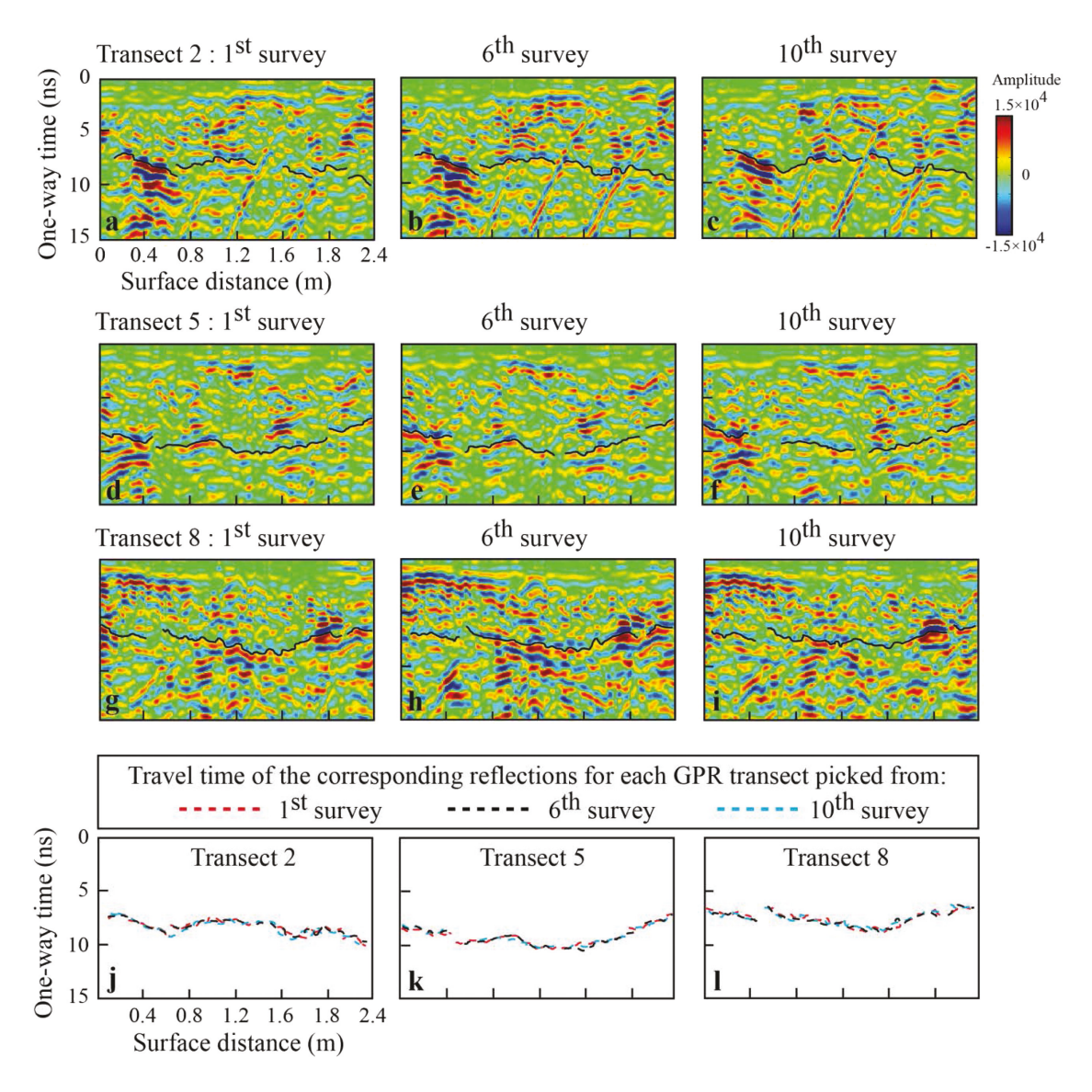


Figure 6. Standardized radargrams collected in the 1st, 6th, and 10th GPR surveys along the (a–c) transect 2, (d–f) transect 5, and (g–i) transect 8. The black lines indicate the travel time pickings of corresponding reflections, which are compared as the same reflector on the radargrams collected in different surveys for the (j-l) transects 2, 5, and 8.

surveys before infiltration produced strong noise signals (Figure 5a). However, subtraction after standardization resulted in much weaker signal differences between the radargrams (Figure 5b). After standardization, the root mean square (RMS) amplitude levels of the subtracted radargrams were  $\sim$ 4 times lower than that of the original radargram before subtraction. The low extent of reflection differences clearly validates the geometric unity between the normalized time-lapse radargrams.

We then compared the differences in travel time pickings of the same reflector elements on the repeated radargrams (Figure 6). Figure 6 shows that although the signal reflectivity changes in different surveys, positions from the same reflectors on different repeated radargrams coincide with each other in both *X* and *Y* directions, regardless of upslope transects (Figure 6j), midslope transects (Figure 6k), or downslope transects (Figure 6l). Figure 6 further demonstrates that the normalized radargrams display a nearly identical geometry.

## 3.4. 3-D Migration

The raw GPR radargram portrays a distorted image of subsurface stratigraphy and buried features. The distortions can be corrected by migration, which traces hyperbolic reflections back to their sources [Daniels, 1996]. Before performing 3-D migration, zero-offset calibration, which compensated for the offset between

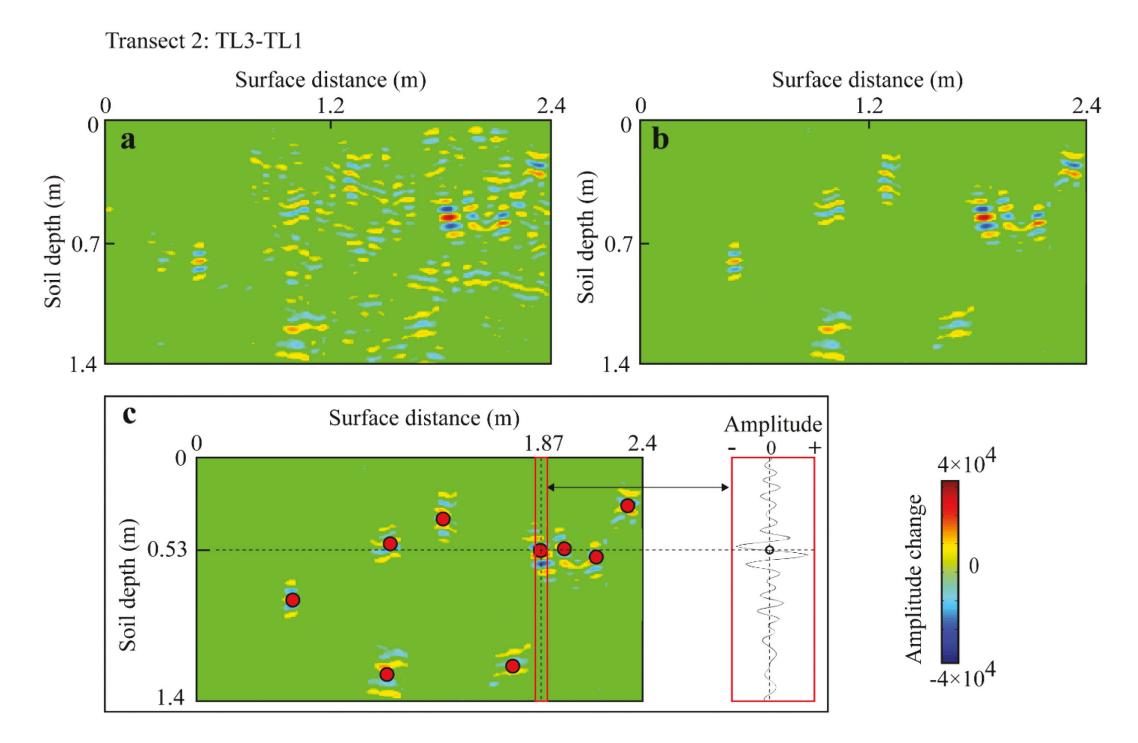


**Figure 7.** Identification and pinpoint of subsurface lateral preferential flow (LPF) radar signatures from time-lapse GPR surveys: (a) Reflection differences between standardized radargrams collected in the first (before infiltration) and third (immediately after infiltration) surveys over the same transect (transect 2). TL stands for time-lapse survey, followed by the number of survey sequence. (b) LPF radar signatures extracted based on the criteria described in the method section, only remaining the strong and isolate signals with at least four successive polarity changes. (c) The location of each LPF radar signature pinpointed based on the signal reflectivity and reflection waveform.

the transmitter and receiver, was achieved by normal-moveout (NMO) correction [*Truss et al.*, 2007]. Then, a new 3-D GPR data volume was generated for each time-lapse survey, and the 3-D Kirchhoff migration was applied to each 3-D data volume. Same as previous studies [e.g., *Truss et al.*, 2007], a constant velocity model (9.12 cm/ns) was used in both the NMO correction and 3-D Kirchhoff migration. An example showing the effects of migration on radargrams is provided in supporting information Appendix Figure 2. All processes for 3-D migration were performed with Reflex Win 6.1. However, the application of migration requires that the velocity structure is known and that the stratigraphy is constructed of laterally homogeneous, constant velocity layers [*Cassidy*, 2009]. If these assumptions are not met, migration may introduce errors. In this case, the application of migration must be very careful.

## 3.5. Lateral Preferential Flow Detection and Mapping

After 3-D migration, the prewetting reference radargrams were subtracted from the corresponding repeats, resulting in changes of radar reflections in each repeated survey. Based on the extents and positions of reflection differences, the occurrences and locations of LPF on each repeated radargram were identified.

Four criteria were carefully established in this study to define LPF radar signatures and pinpoint LPF locations from the scattered reflection differences on the subtracted radargrams (Figure 7):

- 1. Signals with absolute amplitude values smaller than 2 standard deviations of the mean absolute amplitudes of each radargram were filtered, resulting in only the strongest reflection differences remaining (Figure 7b). Preferential flow is related to the heterogeneous and rapid movement of water in the soil, resulting in the higher extent of water variation in locations near preferential flow pathways [Zhu and Lin, 2009; Lin, 2006]. Given the positive correlation between soil water content variation and radar reflection differences [Huisman et al., 2003], preferential flow should lead to stronger reflection differences than those caused by matrix flow.
- 2. Only the signals with at least four successive polarity changes were considered (Figure 7b). Because the main direction of LPF in the sloping landscape is largely lateral downslope, there should be two interfaces (i.e., the upper and lower boundaries) between the LPF pathway and the soil unaffected by LPF, the

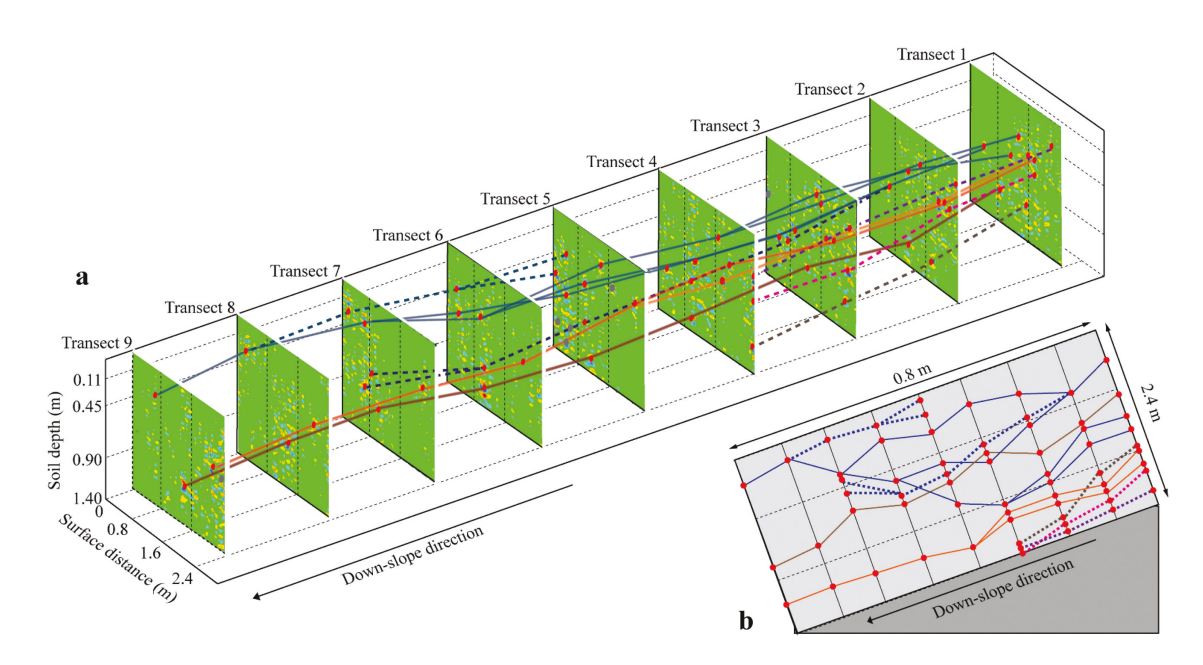


Figure 8. (a) Connection of corresponding subsurface lateral preferential flow (LPF) reflections on neighboring transects along the surveyed hillslope to approximate a 3-D LPF network skeleton (based on the LPF identified in the third time-lapse survey). Red dots indicate the nodes of the LPF network on each subtracted radargram, while gray dots (only few, mainly in transect 5) indicate the LPF signatures that could not be connected between successive transects. (b) 2-D projection of the 3-D LPF network developed in Figure 8a from the upslope transect 1 to the downslope transect 9. Dashed lines represent the LPF pathways that did not cross over the entire surveyed soil, while solid lines represent those LPF pathways that extended across all the survey transects. Different colors indicate different LPF pathways in both Figures 8a and 8b. Note that the scale of the downslope direction is intentionally exaggerated to provide a better visualization of the reconstructed LPF network.

polarity of radar pulses should change twice or more when the radar pulses reached each interface. Moreover, the simulated reflection difference between macropores before and after water bypassing manifest the same pattern of polarity changes (supporting information Appendix Figure 3).

- 3. Only isolated signals with limited reflection difference signals above and below themselves were retained (Figure 7b). Water passing through LPF paths mostly moves along the lateral downslope direction, rather than vertically from the soil surface to deeper soil. Therefore, the reflection difference signals of LPF should be spatially isolated (also see supporting information Appendix Figure 3).
- 4. For each identified LPF radar signature (Figure 7b), the trace where the amplitude reached the maximum was defined as the center trace of the reflection, and the surface distance of this trace was determined as the horizontal location of the corresponding LPF. The position of the zero crossing between the maximum and minimum amplitudes on this trace was defined as the vertical location of this LPF. Thus, the position of each LPF radar signal could be determined (Figure 7c).

Figure 7 provides an example of identifying LPF reflections on a subtracted radargram. After LPF extraction from each subtracted radargram, we then compared the occurrences of LPF at different distances to the infiltration trench (i.e., upslope, midslope, and downslope transects) and at four soil horizons (i.e., Oe-A, Bw, BC, and C horizons).

According to GPR theory, the transmitting antenna generates radar pulses in a beam that travels downward in an elliptical cone [Conyers and Goodman, 1997]. The receiving antenna simultaneously receives both vertical and side reflections within the radiation cone. Such footprint area can be approximated by [Conyers and Goodman, 1997]:

$$A = \frac{\lambda}{4} + \frac{D}{\sqrt{\varepsilon_c + 1}},\tag{4}$$

where A is the long dimension radius of footprint;  $\lambda$  is the center frequency wavelength of radar energy; D is the depth from the ground surface;  $\varepsilon_r$  is the average dielectric constant of scanned medium. Thus, the long dimension radius of the footprint for the chosen 800 MHz antenna increased from 7.86 cm at 20 cm deep to 26.39 cm at 90 cm deep, where most LPF signatures were located. Therefore, it was reasonable to

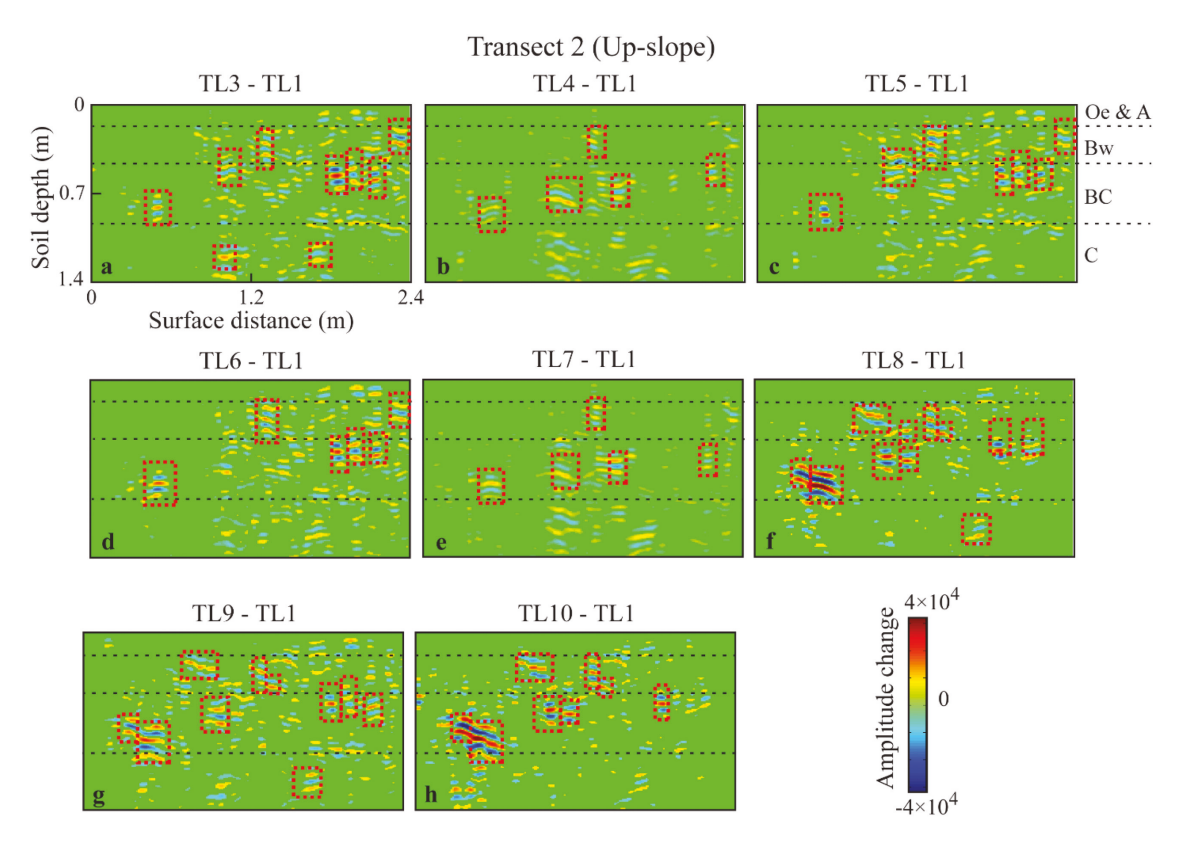


Figure 9. Reflection differences between the prewetting radargram and radargrams collected in subsequent repeated GPR surveys over the same transect 2 (an upslope transect): (a-e) are the subtracted radargrams after the first infiltration, and (f-h) are those after the second infiltration (TL stands for time-lapse survey; TL3 to TL7 refer to 5, 15, 30, 45, and 60 min after the first infiltration; and TL8 to TL10 refer to 5, 15, and 30 min after the second infiltration). Three dashed lines separate each radargram into four horizons: Oe-A, Bw, BC, and C. Red dashed squares highlight the identified signals of subsurface lateral preferential flows (LPF).

link the corresponding reflections of LPF on the densely spaced transects (with an interval spacing of 10 cm) to a possible LPF network on a 3-D scale (Figure 8a).

Connecting LPF radar signatures started from the upslope transects to the downslope transects. For example, if a LPF signature (named as the reference LPF) was detected on the subtracted radargram for the first transect, then a search window (with a diameter of 10 cm) was opened on the subtracted radargram for the second transect. Position of the search window center was maintained as that of the reference LPF on the subtracted radargram for the first transect. Within the search window, the LPF signature that had the shortest distance to the reference LPF was connected to the reference LPF accordingly (Figure 8a). If no corresponding LPF signature was found in the search window, the reference LPF was colored gray, implying that the LPF path either ceased or extended into soils beyond the detection range of GPR. Because the cross-section size of the LPF path was difficult to estimate from the LPF signal, only the skeleton of the LPF network was reconstructed (Figure 8). The 3-D LPF network skeleton thus generated for each time-lapse survey could then be projected into a 2-D scale from the upslope transects to the downslope transects, which made the comparison between different LPF networks more intuitively understandable (Figure 8b). Finally, the LPF networks forming at different stages of the infiltration experiment were reconstructed and compared. The *in situ* soil water content readings were also used to detect LPF signals, and the observed locations of LPF were compared to those identified from time-lapse GPR surveys.

## 4. Results

#### 4.1. Reflection Differences Analysis and LPF Detection

Figure 9 illustrates the occurrences of LPF radar signatures detected on transect 2, as an example of the LPF distribution on the upslope transects. Immediately after the first infiltration, nine LPF radar signatures appeared in a nonuniform spatial distribution (Figure 9a). Fifteen minutes after the first infiltration, the reflection differences with the prewetting background decreased, resulting in five identifiable LPF radar

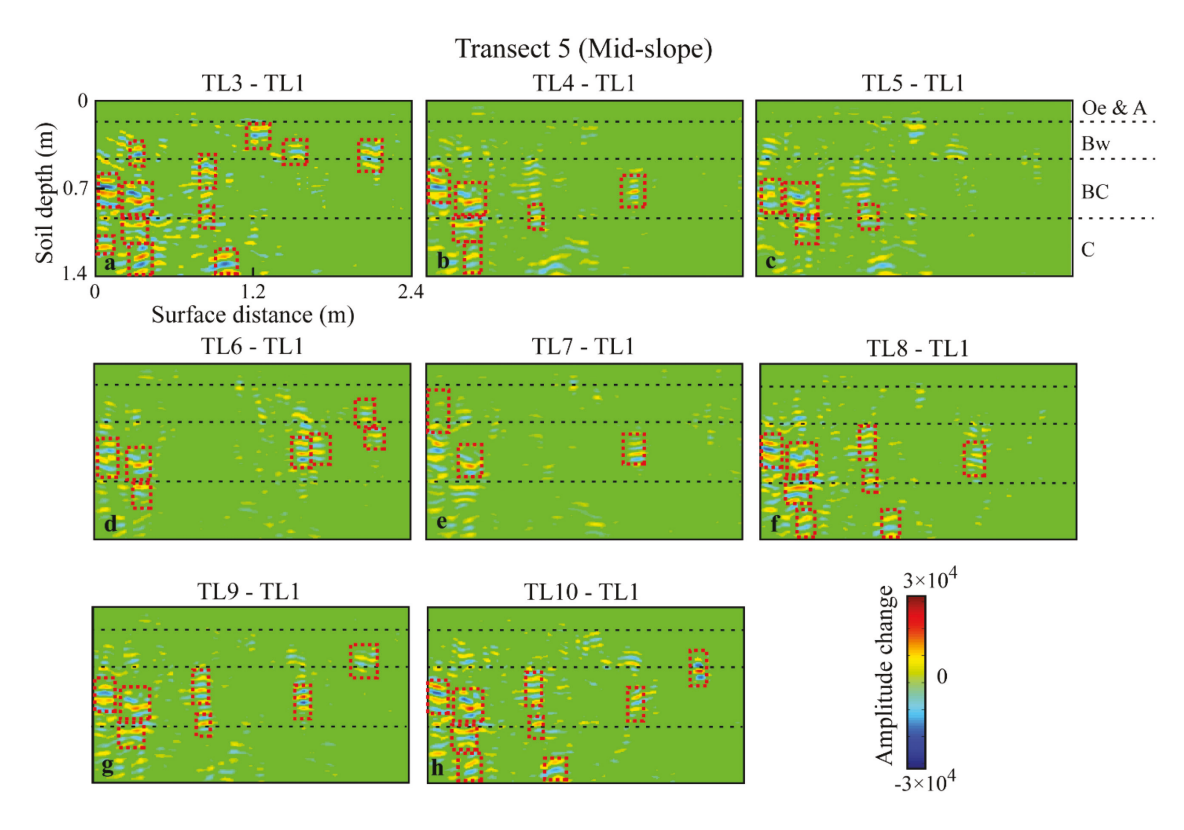


**Figure 10.** Reflection differences between the prewetting radargram and radargrams collected in subsequent repeated GPR surveys over the same transect 5 (a midslope transect): (a-e) are the subtracted radargrams after the first infiltration, and (f-h) are those after the second infiltration (TL stands for time-lapse survey; TL3 to TL7 refer to 5, 15, 30, 45, and 60 min after the first infiltration; and TL8 to TL10 refer to 5, 15, and 30 min after the second infiltration). Three dashed lines separate each radargram into four horizons: Oe-A, Bw, BC, and C. Red dashed squares highlight the identified signals of subsurface lateral preferential flows (LPF).

signatures (Figure 9b). The reflection differences for the fifth and sixth surveys (i.e., 30 and 45 min after the first infiltration, respectively; Figures 9c and 9d) were similar to that observed immediately after the first infiltration, and the LPF signatures were close to those identified in Figure 9a. One hour after the first infiltration, the reflection differences reached the minimum (Figure 9e), indicating that the water had mostly drained out and the soil moisture returned to a state closer to the initial condition.

The number and strength of LPF radar signatures after the second infiltration were higher than those identified after the first infiltration (Figures 9f–9h). Six of the nine LPF signatures detected immediately after the first infiltration reoccurred after the second infiltration (Figures 9a and 9f). The number of LPF signatures gradually decreased after the second infiltration. The strength of LPF radar signatures first decreased at 15 min after the second infiltration (Figure 9g) and later increased again at 30 min (Figure 9h), displaying a similar dynamics to that observed after the first infiltration (Figures 9a–9c).

For midslope transects (represented by transect 5 shown in Figure 10), extensive LPF radar signatures emerged immediately after the first infiltration (Figure 10a). Similar to the LPF dynamics observed for the upslope transects, the following could be observed for the midslope transects (Figure 10): (1) the number and signal strength of LPF signatures declined 15 and 30 min after the first infiltration (Figures 10b and 10c) and then increased 45 min later (Figure 10d) before they reached the minimum 1 h after the first infiltration (Figure 10e); (2) Extensive LPF signatures showed up again after the second infiltration (Figures 10f–10h); (3) The strength of LPF signatures first decreased 15 min after the second infiltration (Figure 10g) and then increased 30 min after the second infiltration (Figure 10h). Unlike the upslope transects, the midslope transects had the following features: (1) the number of LPF occurrences after the second infiltration was lower than that detected immediately after the first infiltration; (2) The LPF locations appeared in the deeper part of the soil profile; (3) The extent of reflection differences for the midslope transects was lower overall.

The downslope transects (represented by transect 8 shown in Figure 11) displayed a quite different scenario in both reflection differences and LPF occurrences: (1) the extent of reflection differences was much lower

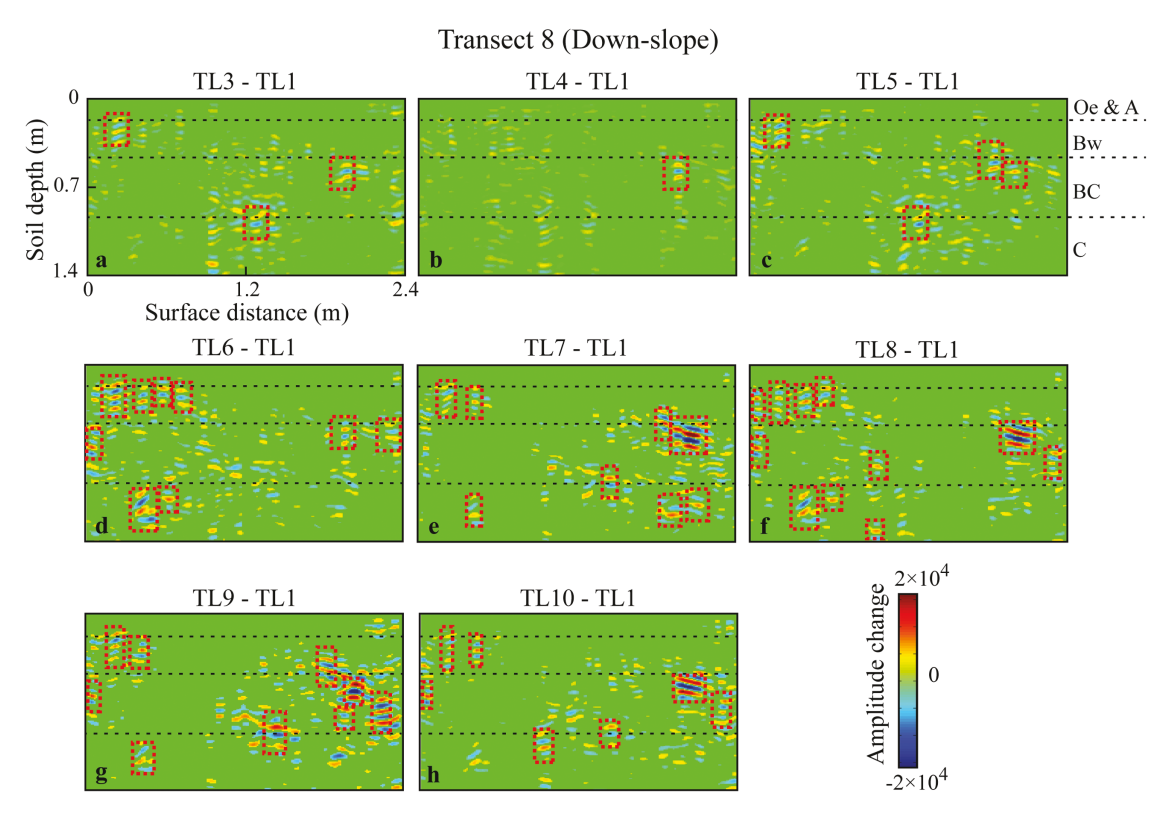


Figure 11. Reflection differences between the prewetting radargram and radargrams collected in subsequent repeated GPR surveys over the same transect 8 (a downslope transect): (a-e) are the subtracted radargrams after the first infiltration, and (f-h) are those after the second infiltration (TL stands for time-lapse survey; TL3 to TL7 refer to 5, 15, 30, 45, and 60 min after the first infiltration; and TL8 to TL10 refer to 5, 15, and 30 min after the second infiltration). Three dashed lines separate each radargram into four horizons: Oe-A, Bw, BC, and C. Red dashed squares highlight the identified signals of subsurface lateral preferential flows (LPF).

throughout the time-lapse surveys after the first infiltration; (2) Only limited LPF radar signatures were detected 5, 15, and 30 min after the first infiltration (Figures 11a, 11b, 11c, and 11i); however, extensive LPF radar signatures remained 1 h after the first infiltration (Figure 11e); (3) After the second infiltration, the number of LPF signatures increased immediately (Figure 11f), and those detected after the first infiltration repeated; (4) The number and strength of LPF signatures gradually decreased from 5 to 15 and to 30 min after the second infiltration (Figures 11f–11h).

The reflection differences and LPF occurrences observed above suggest the following: (1) the distribution of LPF in the study soil is spatially heterogeneous, with most LPF signatures being mapped in the BC horizon, fewer in the Bw and C horizons, and very few in the Oe and A horizons; (2) The number of LPF signatures and the extent of reflection differences varied among independent time-lapse surveys after infiltration, indicating the flow dynamics in the study soil (Figure 12); (3) After the second infiltration, reflection differences and LPF occurrences were higher than what was observed after the first infiltration (Figure 12), but the positions of LPF occurrences after the first infiltration repeated after the second infiltration; (4) A significant decrease in reflection differences and LPF occurrences happened consistently 15 min after the first infiltration; (5) The strength of reflection differences decreased with the increasing distance from the infiltration input trench; (6) After the first infiltration, the number of LPF occurrences declined along the downslope direction, but varied slightly after the second infiltration (Figure 12).

## 4.2. LPF Network Visualization

Figure 13 depicts the dynamics of the 2-D LPF network skeleton after the two infiltrations as revealed by the time-lapse GPR surveys. Immediately after the first infiltration, a complex LPF network appeared, with three LPF pathways connecting the upslope directly to the downslope transects (Figure 13a). The number of nodes in each transect (representing the LPF radar signatures) declined along the downslope direction,

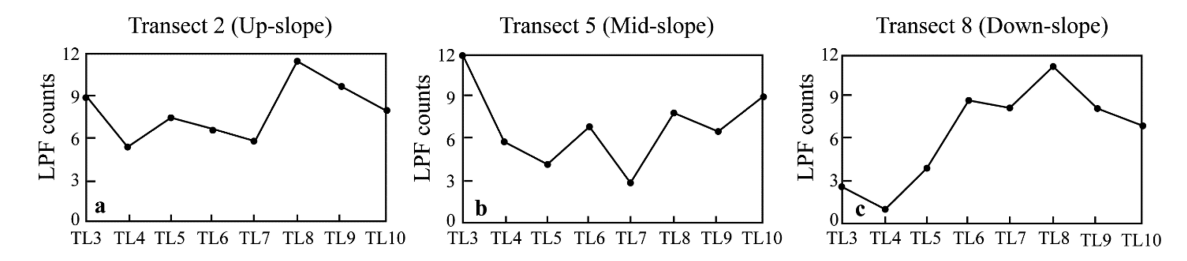


Figure 12. The variations in lateral preferential flow (LPF) counts at different slope sections ((a) upslope; (b) midslope; and (c) downslope) during the repeated GPR surveys. TL stands for time-lapse survey; TL3 to TL7 refer to 5, 15, 30, 45, and 60 min after the first infiltration; and TL8 to TL10 refer to 5, 15, and 30 min after the second infiltration.

especially in the last two transects, indicating only limited pathways for water to reach the downslope area (Figure 13a).

Fifteen and 30 min after the first infiltration, most LPF signatures were shown in the upslope transects, and few LPF pathways extended to the downslope transects, resulting in a simpler LPF network structure than that formed immediately after infiltration (Figures 13b and 13c). Most of these LPF pathways ended at the midslope transects, with only one pathway reaching the downslope area. Based on the similarity of these network structures, we could tell that the LPF networks detected at 15 and 30 min after the first infiltration were the simplified network formed right after the first infiltration, which would represent a wetting up and a drying down cycle (Figures 13a–13c).

However, 45 min after the first infiltration, an extensive LPF network again appeared, with the two LPF pathways connecting the upslope to the downslope transects being similar to that observed right after the first infiltration (Figures 13a and 13d). Unlike that right after the first infiltration, the LPF signatures appearing in Figure 13d varied slightly along the downslope direction, indicating that more water reached the downslope transects (Figure 13d). One hour after the first infiltration, most LPF signals were detected in the downslope transects, and the two LPF pathways connecting the upslope to the downslope transects remained (Figure 13e). When compared to the network formed immediately after the first infiltration, the LPF network structure 1 h later was simpler in the upslope and midslope transects, but more complex in the downslope transects (Figures 13a and 13e).

Right after the second pulse of infiltration, a more complex LPF network appeared, which gradually and slightly decreased over time (Figures 13f–13h). Four LPF pathways extending across the entire survey grid appeared, two of which were similar to that shown right after the first infiltration. The more extensive LPF network developed after the second infiltration suggests that the lubricated lateral preferential flow paths promoted more lateral subsurface flow in the downslope direction (Figures 13f–13h).

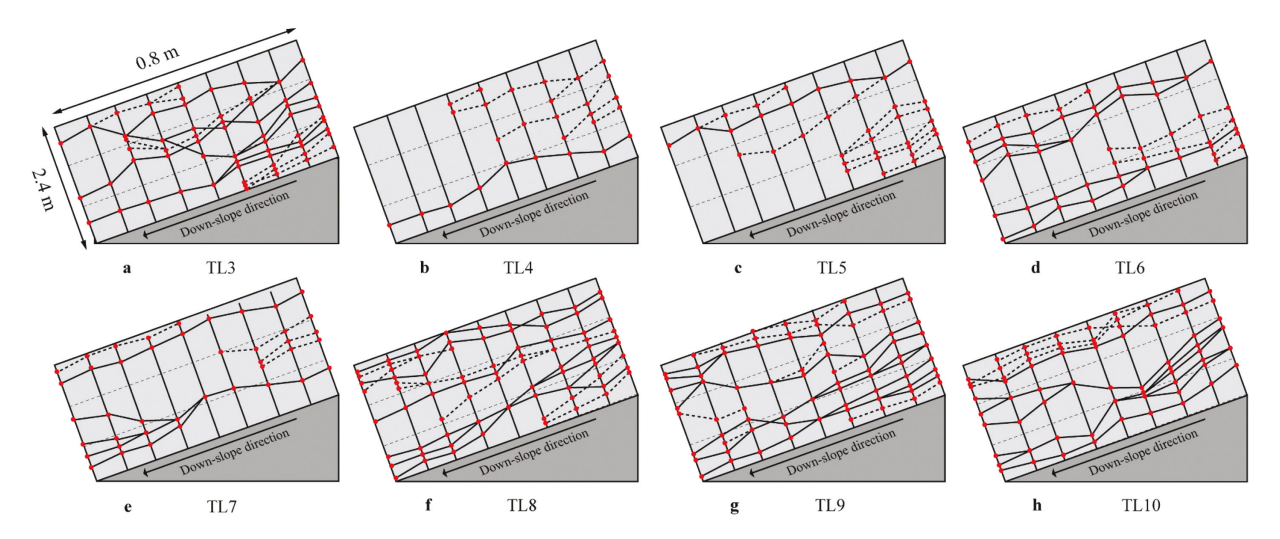
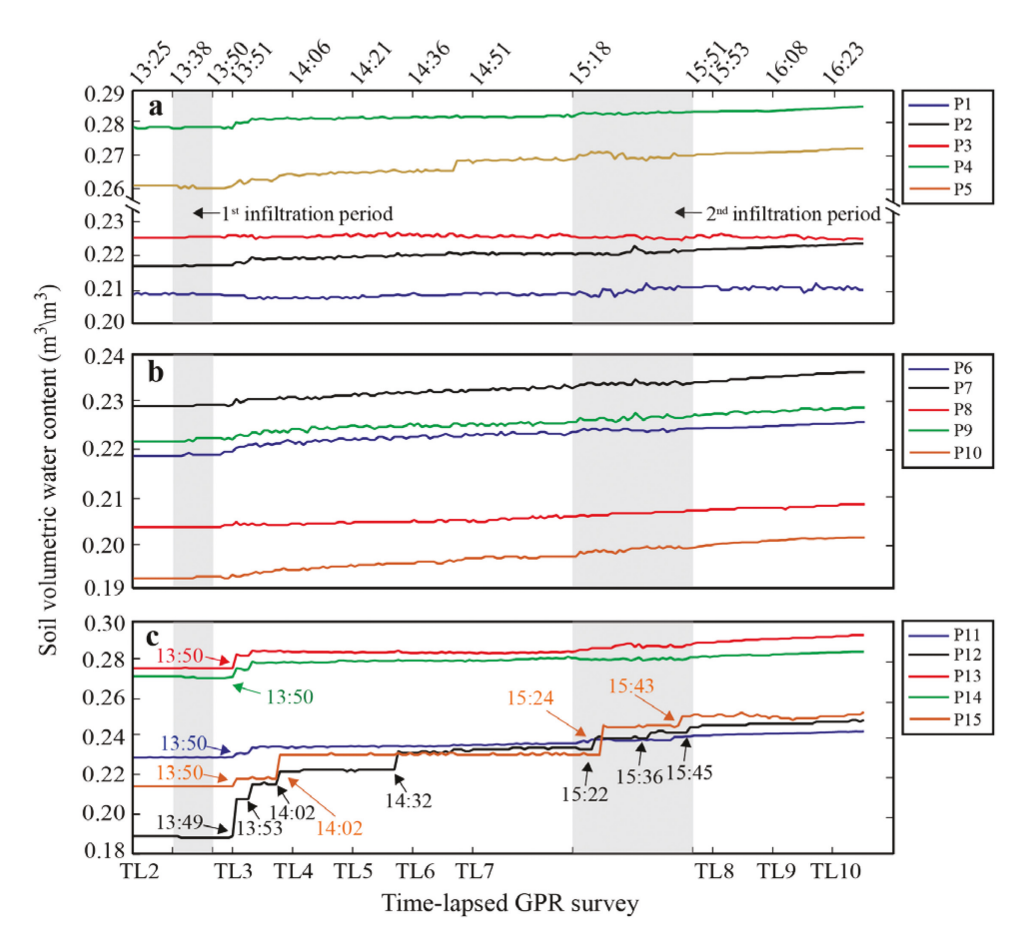


Figure 13. Subsurface lateral preferential flow (LPF) network identified in each of the eight time-lapse GPR surveys (TL stands for time-lapse survey; TL3 to TL7 refer to 5, 15, 30, 45, and 60 min after the first infiltration; and TL8 to TL10 refer to 5, 15, and 30 min after the second infiltration). Red dots represent the locations of LPF signatures identified on each transect. Dashed lines represent the LPF pathways that did not cross over the entire surveyed soil, while solid lines represent those extending across all the surveyed transects. Note that the scale of the downslope direction is intentionally exaggerated to provide a better visualization of the reconstructed LPF networks.



**Figure 14.** Time series of volumetric soil water content recorded in real-time at 10 cm (a), 30 cm (b), and 50 cm (c) depths in the downslope soil pit. Different colors indicate the readings obtained from five independent probes installed at each of the three depths. Arrows indicate the quick jumps of soil water content and their timings, which are likely to be the signals of lateral preferential flows (LPF). TL stands for time-lapse survey; TL3 to TL7 refer to 5, 15, 30, 45, and 60 min after the first infiltration; and TL8 to TL10 refer to 5, 15, and 30 min after the second infiltration.

#### 4.3. Field Soil Water Content Measurements

The real-time soil water contents recorded in the downslope soil pit are plotted in Figure 14. Of the 10 cm probes, probes # 1 and # 3 did not display an apparent response to the infiltration events, whereas probes #2, #4, and #5 showed a gradual increase in soil water content with a low magnitude ( $\sim$ 1% by volume) (Figure 14a). The five 30 cm probes all recorded a slight water content increase of  $\sim$ 0.01 m³/m³ (Figure 14b). Interestingly, five replicate probes at 50 cm depth showed different response patterns to the infiltrations: probe #11, #13, and #14 recorded a gradual soil water content increase with a magnitude of  $\sim$ 0.02 m³/m³ after a moderate jump at 12 min after the beginning of the first infiltration, and probe #12 and #15 recorded several spikes in soil water content (with an increase of  $\sim$ 0.06 m³/m³) during the experimental period (Figure 14c). Such sudden increase of soil water content was not observed by the 10 cm and 30 cm probes (Figures 14a and 14b). The slow soil water content increase is considered to be a result of matrix flow, whereas the quick jump in soil water content is considered to be an indication of LPF occurrence. Although it is also possible that the moderate soil water increase observed in probe #11, #13, and #14 could be caused by matrix flow, the spikes captured by probe #12 and #15 were likely to be the signals of preferential flow. Figure 14 indicates that LPF was dominant in the BC horizon, whereas fewer LPF was detected in the shallower Oe, A, and Bw horizons. These results are consistent with the observations from time-lapse GPR surveys.

## 5. Discussion

# 5.1. Controlling Factors of LPF Network in the Hillslope

The generation, duration, distribution, and structure of LPF network in hillslopes are influenced by subsurface connectivity (e.g., soil macropore network and root distribution) [Newman et al., 1998; Sidle et al., 2001;

Graham and Lin, 2012], hillslope permeability (e.g., soil hydraulic conductivity and impermeable layer) [Uchida et al., 2001; Tromp-van Meerveld and McDonnell, 2006], bedrock layer (including bedrock topography and depth to bedrock) [Freer et al., 1997; Doolittle et al., 2012], and the amount and intensity of water inputs [Newman et al., 1998; Burke and Kasahara, 2011; Zhang et al., 2011]. The principal determinants of the LPF networks observed in the Rushtown soil in this study are discussed below.

#### 5.1.1. Water Input

As the soil near the infiltration trench reached saturation during the first infiltration (Figure 2), the strong interconnected LPF network observed immediately after the first infiltration (Figure 13a) was extensive. After the infiltration stopped, the constant water head in the upslope area disappeared (Figure 2). With water draining both vertically and laterally, the difference in soil water potential between the upslope and the downslope soils decreased, resulting in fewer LPF pathways in the successive surveys (15–60 min after the first infiltration) (Figures 13b–13e). The remaining LPF networks occurred under unsaturated conditions. This suggests that macropores can conduct water in an otherwise unsaturated matrix, supporting the findings reported by *Nimmo* [2012].

During and immediately after the infiltration, the main force driving water passing through the soil laterally was the pressure potential gradient from the upslope area. The continuous water input and stable pressure gradient allowed many preferential flow features to be activated and connected, thus generating extensive LPF network. Once the infiltration input stopped, water stored in the upslope soil would drain downslope under matrix potential and gravimetric potential gradients. Without steady water input and reduced driving force, the complex LPF network started to decrease. This suggests that increasing input water intensity (such as large precipitation) would enhance the initiation of LPF, which is coherent with many observations such as Buttle and McDonald [2002] and Newman et al. [1998]. As the water infiltration stopped, and the stable water head in the infiltration trench disappeared, soil water accumulated in the upslope area near the trench gradually moved further down to the downslope area. At 15 and 30 min after the first infiltration, most LPF pathways were restricted to the upslope area, indicating that the infiltrated water were still near the infiltration trench (Figures 13b and 13c). An intricate LPF network occurred at 45 min after the first infiltration, suggesting that more infiltrated water has entered into the GPR scanned area (Figure 13d). One hour after the first infiltration, more LPF pathways formed in the downslope area, whereas fewer formed in the upslope area, indicating that the infiltrated water has reached and accumulated in the downslope soil (Figure 13e).

#### 5.1.2. Initial Conditions

In addition to water input, the initial soil condition is another important factor controlling LPF occurrence [Graham and Lin, 2011; Nimmo, 2012]. The significant differences between the LPF networks formed immediately after the first and the second infiltrations revealed the positive relationship between the higher antecedent soil water content and the greater likelihood of LPF occurrence (Figures 13a and 13f). This phenomenon is attributed to (1) more connected and "lubricated" LPF pathways under wetter initial soil condition, and (2) more water stored in the initially wetter soil would result in a decrease in the amount of water needed to trigger LPF. Other studies [e.g., Weiler and Naef, 2003; Lin and Zhou, 2008; Kramers et al., 2012] have also reported the higher likelihood of preferential flow occurrence in initially wetter soils.

The initial soil condition also controlled the spatial distribution of LPF pathways. Based on the results from this study, new LPF pathways also occurred immediately after the second infiltration, which were different from those formed immediately after the first infiltration (Figures 13a and 13f).

#### 5.1.3. Hillslope Permeability and Subsurface Hydrologic Connectivity

Soil hydraulic properties have been recognized as important factors influencing LPF [*Lin*, 2006; *Graham and Lin*, 2012]. The heterogeneous hydraulic conductivity and hydrologic connectivity in different soil horizons resulted in two types of LPF network in the soil studied: (1) a network of connected preferential flow pathways, and (2) a network of water flow along permeability contrasts.

The LPF pathways detected in the Bw horizon were a series of connected soil macropores or root channels. The lateral roots were abundant in the Bw horizon in the Rushtown soil (Figure 1b). The laterally orientated root systems increased the hydraulic conductivity and hydrologic connectivity in this soil layer (Figure 1b) and became LPF pathways when the infiltrated water entered the root-soil interface. After the infiltration,

the flow pathways wetted up, allowing water to follow the least resistant path [Lin, 2010; Graham and Lin, 2012]. This type of LPF network was also observed by Noguchi et al. [2001] and Nieber and Sidle [2010].

The formation of LPF network in the BC horizon may be explained by the fill and spill model [*Tromp-van Meerveld and McDonnell*, 2006], in which water flows downslope through a connected network located above a relatively impermeable soil-bedrock interface or a denser soil layer (such as the BC horizon in this study). Fragipans, duripans, clay layers, and other water-restricting soil layers have all been demonstrated to contribute to LPF generation [*Whipkey*, 1965; *Needelman et al.*, 2004; *McDaniel et al.*, 2008; *Lin et al.*, 2008; *Zhu and Lin*, 2009]. In the soil studied, a dense layer started at approximately  $0.6 \sim 0.8$  m depth, which accounted for the most abundant LPF occurrences in the BC horizon (Figure 1b). This dense layer was also observed by our previous studies at this site [*Lin*, 2006; *Zhang et al.*, 2014]. The relatively higher rock fragment percentage in the C horizon (Figure 1b) also suggests that LPF in this horizon might have occurred at the soil-rock fragment interface.

## 5.2. Effectiveness and Limitation of the Time-Lapse GPR Surveys in Mapping LPF Network

Considerable efforts were made in this study to improve the repeatability of radargrams collected from time-lapse GPR surveys. First of all, controlled infiltration took place 0.5 m upslope from the GPR survey area rather than directly over the survey grid. As a large proportion of infiltrated water likely has percolated downward vertically into the initially relatively dry ground, and only a small portion of infiltrated water moved laterally in downslope. This ensured a limited increase in soil water content (Figure 14) and thus confined the extent of travel time shift on repeated radargrams (supporting information Appendix Table 1). In our case, the average increase recorded in the downslope soil water probes was less than 0.02 m³/m³ (from initial 0.23 to postwetting 0.25 m³/m³). According to the Topp equation, the dielectric constant of soil with volumetric water content at 0.23 m³/m³ is 11.96, and the corresponding GPR wave velocity is 8.68 cm/ns (calculated by equation (1)). When soil water content increases to 0.25 m³/m³, soil dielectric constant changes to 13.28, and the corresponding wave velocity decreases to 8.23 cm/ns. Therefore, within the temporal scale of this study, the largest depth variation caused by electromagnetic velocity change is less than 7 cm, which ensures the accuracy of LPF locations mapped by the time-lapse GPR.

GPR data postprocessing was also considerably optimized in this study (Figure 3). The basic processing steps eliminated the impact of ground topography, compensated radar energy attenuation, and increased the signal/noise ratio. Through radargram standardization, repeated radargrams were normalized into an "identical" geometry (Figures 5 and 6), which enhanced the comparability between repeated radargrams (also see supporting information Appendix Figure 4). After performing subtraction between the prewetting and postwetting radargrams, we retained the significant reflection variations by setting a threshold value, which eliminated the noise signals brought about by possible geometric mismatches (Figure 7). Based on the nature of LPF pathways, only those isolated signal differences with successive polarity changes were defined as the LPF radar signatures (Figure 7). Finally, given that the small interval spacing between transects could be overlapped within the footprint of radar energy beam, it was reasonable to connect the adjacent LPF radar signatures into a LPF network, which could not be achieved by the travel time delay analysis used in previous time-lapse GPR surveys [e.g., *Truss et al.*, 2007].

Based on the observations of the time-lapse GPR, most LPF occurred in the BC horizon, and few appeared in the near surface Oe and A horizons (Figures 9–11). This was proven by the real-time soil water content recorded in the downslope soil pit (Figure 14). The quick jumps noted in soil water content were consistent with the formation of the LPF network. Although the downslope soil moisture records could not directly validate the LPF network mapped by GPR, real-time soil water monitoring was the best available method to directly detect possible subsurface water flow. There is no other means that is currently available to directly prove the time-lapse nature of LPF.

Nevertheless, as the first attempt to map a LPF network using GPR in the field, our method still has some limitations. These are summarized as follows: (1) the LPF radar signatures was manually selected on the subtracted radargrams. How this may affect the interpretation of radar data is uncertain, and thus more efforts should be made to develop automatic LPF identification algorithm; (2) The spatial pattern of LPF network inferred by GPR has not been validated directly in the field. Thus, future work should combine tracer infiltration, time-lapse GPR, and small-scale excavation to provide fuller validation of the presented data postprocessing method; (3) Although the surface soil water content can be approximated by the reflection from

the air-soil interface [Davis and Annan, 2002; Redman et al., 2002], it is still challenging to quantitatively estimate soil water content from the subsurface reflection information, which limits the quantitative analysis of soil hydraulic processes using GPR; (4) Only the macropore LPF that extended approximately parallel to the slope direction was identified in the LPF network; and (5) Diverse field conditions may restrict the application of GPR in certain hillslopes. The best GPR detection quality is achieved in dry sandy soil [Guo et al., 2013]. However, in some hillslopes, relatively high soil water content and clay content may intensify the attenuation of GPR energy, leading to a limited detection range. In addition, topographic roughness could impede conducting GPR surveys in some hillslopes. The representativeness of the GPR detection results is limited to the size of the investigation area. The feasibility of applying our methodology for mapping vertical preferential flow pathways and other types of LPF in different landscapes (e.g., flat ground) would require further development and testing in the future.

# **6. Summary and Conclusions**

Through combining artificial infiltration with time-lapse GPR surveys in a hillslope, we have established a new protocol for noninvasive detection of LPF and its network. Our field experimental setup ensured that only a small increase of soil water content could occur in the study soil, thus minimizing the possible travel time shift on GPR radargrams after water infiltration. The enhanced radar data postprocessing procedures developed in this study provided a means to normalize repeated radargrams to the same geometry. The improved repeatability of time-lapse radargrams thus facilitated the comparison of reflection differences before and after wetting and the detection of the LPF signatures.

Most LPF pathways were detected in the BC horizon of the study soil. The LPF network varied in different time-lapse surveys due to its formation and variation being controlled by different initial soil water contents, soil hydraulic conductivity, and subsurface hydrologic connectivity. The locations of LPF occurrence mapped by time-lapse GPR surveys were validated by the real-time monitoring of soil water. Two types of LPF networks were identified: the network at the soil permeability contrast and the network formed via a series of connected preferential flow paths. Overall, the results of this study have improved our understanding of LPF network formation and its complexity and thus facilitated the formulation and testing of different possible conceptualizations of subsurface flow processes.

The newly established field experimental setup and GPR data postprocessing have increased the robustness and accuracy of reflection difference analysis between time-lapse radargrams, thus providing an effective and noninvasive means of detecting *in situ* LPF networks. The results from this study can significantly improve our ability to study the initiation, spatial distribution, and dynamics of LPF in hillslopes and offer an attractive means of revealing the complexity of subsurface hydrological processes in diverse soil landscapes.

#### Acknowledgments

This research was supported in part by the U.S. National Science Foundation through the Shale Hills Critical Zone Observatory (grant EAR-0725019, PI: C. Duffy; and EAR 12-39285, EAR 13-31726, Pl: S. Brantley), and by the National Natural Science Foundation of China (grant 41001239, grant 41401378) and the Fundamental Research Funds for the Central Universities. We gratefully thank three anonymous reviewers and the Associate Editor for their valuable comments and suggestions that have helped improve the quality of this paper. The corresponding author (Henry Lin) may be contacted for access to the data generated in this study.

## References

al Hagrey, S. A. (2007), Geophysical imaging of root-zone, trunk, and moisture heterogeneity, *J. Exp. Bot., 58*, 839–854.

Allaire, S. E., S. Roulier, and A. J. Cessna (2009), Quantifying preferential flow in soils: A review of different techniques, *J. Hydrol.*, 378, 179–204.

Anderson, A. E., M. Weiler, Y. Alila, and R. O. Hudson (2009), Dye staining and excavation of a lateral preferential flow network, *Hydrol. Earth Syst. Sci.*, 13, 935–944.

Annan, A. P. (2005), Ground-penetrating radar, in *Near-Surface Geophysics, Invest. Geophys.*, vol. 13, edited by D. K. Butler, chap. 11, pp. 357–438, Soc. of Explor. Geophys., Tulsa, Okla.

Boschetti, F., M. D. Dentith, and R. D. List (1996), A fractal-based algorithm for detecting first arrivals on seismic traces, *Geophysics*, *61*, 1005–1102

Burke, A. R., and T. Kasahara (2011), Subsurface lateral flow generation in aspen and conifer-dominated hillslope of a first order catchment in northern Utah, *Hydrol. Processes*, 25, 1407–1417.

Buttle, J. M., and D. J. McDonald (2002), Coupled vertical and lateral preferential flow on a forested slope. Water Resour. Res., 38(5), 1060, doi:10.1029/2001WR000773.

Cassidy, N. J. (2009), Ground penetrating radar data processing, modeling and analysis, in *Ground Penetrating Radar, Theory and Applications*, edited by H. Jol, pp. 164–165, Elsevier, Amsterdam, Netherlands.

Conyers, L. B., and D. Goodman (1997), Ground-Penetrating Radar: An Introduction for Archaeologist, Altamira Press, Walnut Creek, Calif. Daniels, D. J. (1996), Surface-Penetrating Radar, Inst. of Electr. Eng., London, U. K.

Davis, J. L., and A. P. Annan (2002), Ground penetrating radar to measure soil water content, in *Methods of Soil Analysis, Soil Science Society of America Book Ser. 5, Part 4*, pp. 446–463, Soil Science Society of America, Madison, Wis.

Doolittle, J., Q. Zhu, J. Zhang, L. Guo, and H. S. Lin (2012), Geophysical investigations of soil-landscape architecture and its impacts on subsurface flow, in *Hydropedology: Synergistic Integration of Soil Science and Hydrology*, edited by H. Lin, pp. 413–448, Elsevier, Mass.

- Freer, J., J. J. McDonnell, K. J. Beven, D. Brammer, D. Burns, R. P. Hooper, and C. Kendall (1997), Topographic controls on subsurface storm flow at the hillslope scale for two hydrologically distinct small catchments, *Hydrol. Processes*, 11, 1347–1352.
- Gormally, K. H., M. S. McIntosh, A. N. Mucciardi, and G. W. McCarty (2011), Ground-penetrating radar detection and three-dimensional mapping of lateral macropores: II. Riparian application, *Soil Sci. Soc. Am. J.*, 75, 1236–1243.
- Graham, C. B., and H. S. Lin (2011), Controls and frequency of preferential flow occurrence: A 175-event analysis, Vadose Zone J., 10, 816–831.
- Graham, C. B., and H. S. Lin (2012), Subsurface flow networks at the hillslope scale: Detection and modeling, in *Hydropedology: Synergistic Integration of Soil Science and Hydrology*, edited by H. Lin, pp. 559–594, Elsevier, Mass.
- Graham, C. B., R. A. Woods, and J. J. McDonnell (2010), Hillslope threshold response to rainfall: (1) A field based forensic approach, J. Hydrol., 393, 65–76
- Grote, K., S. Hubbard, and J. Harvey (2005), Evaluation of infiltration in layered pavements using surface GPR reflection techniques, *J. Appl. Geophys.*, 57, 129–153.
- Guo, L., J. Chen, X. H. Cui, B. H. Fan, and H. S. Lin (2013), Application of ground penetrating radar for root detection and quantification: A review, *Plant Soil*, 362, 1–23.
- Holden, J. (2004), Hydrological connectivity of soil pipes determined by ground-penetrating radar tracer detection, *Earth Surf. Processes Landforms*, 29, 437–442.
- Holden, J. and T. P. Burt (2002), Piping and pipeflow in a deep peat catchment, Catena, 48, 163–199.
- Huisman, J. A., S. S. Hubbard, J. D. Redman, and A. P. Annan (2003), Measuring soil water content with ground penetrating radar: A review, *Vadose Zone J.*, 2, 476–491.
- Jones, J. (2010), Soil piping and catchment response, Hydrol. Processes, 24, 1548-1566.
- Kramers, G., N. M. Holden, and F. Brennan (2012), Water content and soil type effects on accelerated leaching after slurry application, *Vadose Zone J.*, 11, 244–257, doi:10.2136/vzj2011.0059.
- Lin, H. S. (2006), Temporal stability of soil moisture spatial pattern and subsurface preferential flow pathways in the Shale Hills catchment, *Vadose Zone J.*, 5, 317–340.
- Lin, H. S. (2010), Linking principles of soil formation and flow regimes, J. Hydrol., 393, 3–19.
- Lin, H. S. and X. B. Zhou (2008), Evidence of subsurface preferential flow using soil hydrologic monitoring in the shale hills catchment, *Eur. J. Soil Sci.*, *59*, 34–49.
- Lin, H. S., E. Brook, P. McDaniel and J. Boll (2008), Hydropedology and surface/subsurface runoff processes, in *Encyclopedia of Hydrologic Sciences*, edited by M. G. Anderson, pp. 1–25, Wiley, Chichester, U. K., doi:10.1002/0470848944.hsa306.
- Luxmoore, R. J., P. M. Jardine, G. V. Wilson, J. R. Jones, and L. W. Zelazny (1990), Physical and chemical controls of preferred path flow through a forested hillslope, *Geoderma*, 46, 139–154.
- McDaniel, P. A., M. P. Regan, E. Brooks, J. Boll, S. Barndt, A. Falen, S. K. Young, and J. E. Hammel (2008), Linking fragipans, perched water tables, and catchment-scale hydrological processes, *Catena*, 73, 166–173.
- Needelman, B. A., W. J. Gburek, G. W. Petersen, A. N. Sharpley, and P. J. A. Kleinman (2004), Surface runoff along two agricultural hillslopes with contrasting soils, Soil Sci. Soc. Am. J., 68, 914–923.
- Newman, B. D., A. R. Campbell, and B. P. Wilcox (1998), Lateral subsurface flow pathways in a semiarid ponderosa pine hillslope, *Water Resour. Res.*, 34, 3485–3496.
- Nieber, J. L., and R. C. Sidle (2010), How do disconnected macropores in sloping soils facilitate preferential flow?, *Hydrol. Processes*, 24, 1582–1594.
- Nimmo, J. R. (2012), Preferential flow occurs in unsaturated conditions, Hydrol. Processes, 26, 786–789.
- Noguchi, S., Y. Tsuboyama, R. C. Sidle, and I. Hosoda (2001), Subsurface runoff characteristics from a forest hillslope soil profile including macropores, Hitachi Ohta, Japan, *Hydrol. Processes.*, 15, 2131–2149.
- Redman, J. D., J. L. Davis, L. W. Galagedara, and G. W. Parkin (2002), Field studies of GPR air launched surface reflectivity measurements of soil water content, *Proc. SPIE Int. Soc. Opt. Eng.*, 4758, 156–161.
- Roth, C. H., M. A. Malicki, and R. Plagge (1992), Empirical evaluation of the relationship between soil dielectric constant and volumetric water content as the basis for calibrating soil moisture measurements by TDR, J. Soil Sci., 43, 1–13.
- Schmelzbach C., J. Tronicke, and P. Dietrich (2012), High-resolution water content estimation from ground-penetrating radar reflection data by impedance inversion, *Water Resour. Res., 48*, W08505, doi:10.1029/2012WR011955.
- Sidle, R. C., S. Noguchi, Y. Tsuboyama, and L. Karin (2001), A conceptual model of preferential flow systems in forested hillslopes: Evidence of self-organization, *Hydrol. Processes*, 15, 1675–1692.
- Topp, G. C., J. L. Davis, and A. P. Annan (1980), Electromagnetic determination of soil water content: Measurements in coaxial transmission lines, *Water Resour. Res.*, 16, 574–582.
- Trinks, I., D. Wachsmuth, and H. Stümpel (2001), Monitoring water flow in the unsaturated zone using georadar, First Break, 19, 679–684.
- Tromp-van Meerveld, H. J., and J. J. McDonnell (2006), Threshold relations in subsurface stormflow: 1. A 147-storm analysis of the Panola hillslope, *Water Resour. Res.*, 42, W02410, doi:10.1029/2004WR003778.
- Tromp-van Meerveld, H. J., N. E. Peters, and J. J. McDonnell (2007), Effect of bedrock permeability on subsurface stormflow and the water balance of a trenched hillslope at the Panola Mountain Research Watershed, Georgia, USA, *Hydrol. Processes*, 21, 750–769.
- Truss, S., M. Grasmueck, S. Vega, and D. A. Viggiano (2007), Imaging rainfall drainage within the Miami oolitic limestone using high-resolution time-lapse ground-penetrating radar, *Water Resour. Res.*, 43, W03405, doi:10.1029/2005WR004395.
- Tsuboyama, Y., R. C. Sidle, S. Noguchi, and I. Hosoda (1994), Flow and solute transport through the soil matrix and macropores of a hillslope segment, Water Resour. Res., 30, 879–890.
- Uchida, T., K. Kosugi, and T. Mizuyama (2001), Effects of pipeflow on hydrological process and its relation to landslide: A review of pipeflow studies in forested headwater catchments, *Hydrol. Processes*, *15*, 2151–2174.
- Uhlenbrook, S. (2006), Catchment hydrology—A science in which all processes are preferential, Hydrol. Processes, 20, 3581–3585.
- van Verseveld, W. J., J. J., McDonnell, and K. Laitha (2009), The role of hillslope hydrology in controlling nutrient loss, *J. Hydrol.*, 367, 177–187.
- Versteeg, R. (2002), Near-real time imaging of subsurface processes using geophysics, in Expanded Abstracts of the 72nd Annual International Meeting: Society of Exploration Geophysics, pp. 1500–1503, Soc. of Explor. Geophys., Salt Lake City, Utah.
- Weiler, M., and F. Naef (2003), Simulating surface and subsurface initiation of macropore flow, *J. Hydrol.*, *273*, 139–154.
- Weiler, M., J. J. McDonnell, I. T. Meerveld, and T. Uchida (2006), Subsurface stormflow, in *Encyclopedia of Hydrological Sciences*, vol. 3, Part 10, edited by M. G. Anderson and J. J. McDonnell, pp. 1719–1732, John Wiley, Chichester, U. K.
- Whipkey, R. Z. (1965), Subsurface storm flow from forested slopes, Bull. Int. Assoc. Sci. Hydrol., 2, 74–85.

- Wilcox, B. P., B. D. Newman, D. Bres, D.W. Davenport, and K. Reid (1997), Runoff from a semiarid ponderosa pine hillslope in New Mexico, Water Resour. Res., 33, 2301–2314.
- Yoder, R. E., R. S. Freeland, J. T. Ammons, and L. L. Leonard (2001), Mapping agricultural fields with GPR and EMI to identify offsite movement of agrochemicals, *J. Appl. Geophys.*, 47, 251–259.
- Zhang, B., J. L. Tang, Ch. Gao, and H. Zepp (2011), Subsurface lateral flow from hillslope and its contribution to nitrate loading in streams through an agricultural catchment during subtropical rainstorm events, *Hydrol. Earth Syst. Sci.*, 15, 3153–3170.
- Zhang, J., H. Lin and J. Doolittle (2014), Soil layering and preferential flow impacts on seasonal changes of GPR signals in two contrasting soils, *Geoderma*, 213, 560–569.
- Zhu, Q., and H. S. Lin (2009), Simulation and validation of concentrated subsurface lateral flow paths in an agricultural landscape, *Hydrol. Earth Syst. Sci.*, 13, 1503–1518.
- Zhu, Q., H. S. Lin and J. Doolittle (2010a), Repeated electromagnetic induction surveys for determining subsurface hydrologic dynamics in an agricultural landscape, *Soil Sci. Soc. Am. J.*, *74*, 1750–1762.
- Zhu, Q., H. S. Lin, and J. Doolittle (2010b), Repeated electromagnetic induction surveys for improving soil mapping in an agricultural land-scape, Soil Sci. Soc. Am. J., 74, 1763–1774.